Petroleum Science 23 (2026) 7037–7051

Contents lists available at ScienceDirect

Petroleum Science

journal homepage: www.keaipublishing.com/en/journals/petroleum-science

Original Paper

Interfacial adhesive behaviors between clathrate hydrates and mineral microparticles: AFM measurements and capillary bridge modeling

Wei Li [a,b], Zhi-Chao Liu [a,b], Feng-Yi Mi [c], Fang-Yu Shi [a], Jiang-Tao Pang [d], Zheng-Tao Tao [a], Jia-Ni Hong [e], Fu-Long Ning [a,b,f,*]

[a] Faculty of Engineering, China University of Geosciences, Wuhan, 430074, Hubei, China
[b] National Center for International Research on Deep Earth Drilling and Resource Development, China University of Geosciences, Wuhan, 430074, Hubei, China
[c] Key Laboratory of Solid Waste Treatment and Resource Reuse, Ministry of Education, Southwest University of Science and Technology, Mianyang, 621010, Sichuan, China
[d] State Key Laboratory of Geomechanics and Geotechnical Engineering Safety, Institute of Rock and Soil Mechanics, Chinese Academy of Sciences, Wuhan, 430071, Hubei, China
[e] International Center for Quantum Materials, School of Physics, Peking University, Beijing, 100871, China
[f] School of Mechanical Engineering and Electronic Information, China University of Geosciences, Wuhan, 430074, Hubei, China

ARTICLE INFO

Article history:
Received 22 January 2026
Received in revised form
29 April 2026
Accepted 7 September 2026
Available online 10 September 2026

Edited by Xiu-Fang Hu

Keywords:
Atomic force microscope
Clathrate hydrate
Adhesion force
Mineral microparticles
Capillary bridge

ABSTRACT

The industrial development of natural gas hydrate, a promising clean energy resource, is hindered by key technical challenges such as formation degradation, reservoir instability, and sand production. Understanding the interfacial adhesive behaviors between hydrates and sediment particles on the order of tens of micrometers is essential to address these engineering challenges, as the strength of these adhesion forces directly governs the mobilization of sediment particles and thus controls the macroscopic risks of sand production and reservoir destabilization. Accordingly, a custom-made cryogenic atomic force microscope was used to probe the adhesion forces between mineral microparticles and clathrate tetrahydrofuran hydrate at the microscale. The results indicate that the adhesion behavior at the hydrate–mineral interface is governed by mineral particle size, temperature, contact force, and contact time. Particularly, as the mineral particle size and contact force increase, a greater indentation depth and an increased amount of decomposition liquid significantly strengthen the adhesion force. Higher temperatures also enhance adhesion, primarily due to the thickening of the quasi-liquid layer produced by the premelting of hydrate crystals even below the phase equilibrium temperature. Notably, the adhesion force is time-dependent. Under compression, the competing processes of hydrate decomposition and formation cause the force to exhibit a non-monotonic evolution, initially increasing to a peak and then declining with prolonged contact time. Finally, by incorporating indentation depth and quasi-liquid layer thickness, we optimized a capillary bridge model that reveals microscale plastic deformation at the hydrate–sediment interface under compression. These microscale insights directly link interfacial adhesion mechanisms to the security risks in hydrate development, offering a scientific basis for risk mitigation.

© 2026 The Authors. Publishing services by Elsevier B.V. on behalf of KeAi Communications Co. Ltd. This is an open access article under the CC BY license (http://creativecommons.org/licenses/by/4.0/).

1. Introduction

Clathrate hydrates are non-stoichiometric crystalline compounds, commonly formed by water and small guest molecules under certain temperature and pressure conditions (He et al., 2025). The most well-known clathrate hydrates are those in

* Corresponding author
E-mail address: nflzx@cug.edu.cn (F.-L. Ning).
Peer review under the responsibility of China University of Petroleum (Beijing).

https://doi.org/10.1016/j.petsci.2026.09.009
1995-8226/© 2026 The Authors. Publishing services by Elsevier B.V. on behalf of KeAi Communications Co. Ltd. This is an open access article under the CC BY license (http://creativecommons.org/licenses/by/4.0/).

which natural gas serves as guest molecules, referred to as natural gas hydrates. Due to their abundant reserves and potential for reducing carbon emissions, hydrates are considered a promising unconventional energy resource (Pang et al., 2025). To optimize energy structures and achieve carbon neutrality (Yu et al., 2021; Cheng et al., 2023), researchers worldwide have conducted fruitful research on hydrate exploration and development (Yamamoto et al., 2019; Ye et al., 2020). However, in addition to increasing natural gas production (Guo et al., 2024), there remain several unsolved safety issues, hindering commercial hydrate exploitation (Ning et al., 2012; Kong et al., 2025).

As drilling activities continue, the macromechanical properties of hydrate-bearing sediments tend to deteriorate, leading to adverse reservoir response behaviors such as wellbore instability or sand production (Li et al., 2023b; Zhao et al., 2024), thus constraining hydrate energy development. The mechanical degradation of hydrate reservoirs is mainly attributed to changes in interfacial interactions between hydrates and sediment particles (Qureshi et al., 2022; Wang et al., 2022a). Among these, clarifying the interfacial adhesion behaviors between them is critical for improving the accuracy of sand production prediction and wellbore stability analysis at the microscale, since hydrates in reservoirs predominantly exist in pore media composed of micro- and nanometer-sized particles. These interfacial behaviors are sensitive to the effects of the complicated natural reservoir environment (e.g., sediment particle size and temperature) and operational parameters (e.g., contact force and loading rate) (Li et al., 2021, 2026a; Huang et al., 2023). In addition to their role in energy resource exploitation, hydrates are also critical to submarine geohazards and climate change (Kim, 2022; Thornton and Stranne, 2023). Hydrates can function as a cementing agent, binding sediment particles together (Guo et al., 2023). When dissociated by natural or anthropogenic disturbances, hydrates tend to weaken sediment strength, potentially triggering large-scale submarine landslides, such as the Storegga Slide off the coast of Norway, one of the largest known submarine landslides (Hill et al., 2012). Such events can release substantial amounts of methane, a potent greenhouse gas, into the water column and atmosphere, thereby contributing to a positive feedback loop that exacerbates global warming (Kim, 2022). Furthermore, the utilization of hydrate technology for natural gas storage and carbon dioxide capture in porous media materials relies on the interfacial adhesive or cementation behaviors between hydrates and solid surfaces (Farrando-Perez et al., 2022; Yang et al., 2025). These phenomena further highlight the significance of understanding and regulating interfacial adhesion force for effective hydrate management and application. The physical basis for this sensitivity lies in the capillary bridge formed at the microscale hydrate–particle interface (Fig. 1) (Aman and Koh, 2016; Luo et al., 2024). During contact and separation, a capillary bridge can form between the hydrate and the solid particle, generating an additional attractive force (Nguyen et al., 2021). The strength of this capillary bridge is highly sensitive to interfacial conditions, such as temperature, surface morphology, particle size, contact force, and contact time, because these factors affect its geometry and stability (Phan et al., 2022; Luo et al., 2024). Therefore, clarifying how these variables regulate capillary bridge formation is essential for understanding the microscopic origin of hydrate–particle adhesion.

Most studies of adhesion force between hydrates and solid materials at the microscale are conducted using the micromechanical force (MMF) apparatus (Li et al., 2026a; Luo et al., 2026). In the initial study, Taylor et al. (2007) observed that the adhesion forces between tetrahydrofuran (THF) hydrate particles increased with higher temperature and longer contact time. Furthermore, many researchers have concluded that modifying surface properties, such as roughness, morphology, and wettability, can decrease the adhesion force between hydrates and solid materials, thereby reducing the risks of hydrate aggregation (Phan et al., 2022; Luo et al., 2026). However, the sizes of hydrate particles or other solid media measured by the MMF apparatus usually range from 300 to 500 μm (Aman et al., 2011), which are orders of magnitude larger than those of the actual hydrate or sediment particles found in oil/gas pipelines and hydrate reservoirs (Zhang et al., 2024). Wang et al. (2020) confirmed that the adhesion force of hydrate was linearly correlated with the particle radius by MMF. Thus, interfacial adhesion between hydrates and solid materials, such as steel pipelines, porous materials, and sediment particles, at scales smaller than hundreds of microns (including the nanoscale), is also crucial (Nguyen et al., 2022; Lin et al., 2023). Nevertheless, few technologies are currently capable of probing the micromechanical behavior of hydrate systems, particularly the interfacial interaction between hydrates and skeleton particles at the micro/nano scale.

Recently, the atomic force microscope (AFM) has been successfully applied to identify the interfacial characteristics and mechanical properties of ice from a microscopic perspective (Hong et al., 2024), which provides a promising methodology for studying the basic scientific issues in the field of hydrates (Li et al., 2023a, 2024). To explore this, we modified a cryogenic AFM system to accurately investigate the interfacial adhesive behaviors between clathrate hydrates and single sediment particles. The effects of hydrate surface morphology, temperature, and mineral microparticle size, along with contact force, contact time, and loading/unloading rate, on adhesion forces between hydrates and mineral microparticles were systematically examined. Additionally, by accounting for indentation characteristics, a capillary bridge model was optimized to demonstrate the plastic deformation at hydrate–sediment interfaces under microscale compression. This pioneering study provides a deeper understanding of the adhesive mechanisms between hydrates and sediment particles at the micro/nano scale. Based on these insights, further research is expected to focus on analyzing the mechanisms of engineering and geohazard phenomena, thereby supporting safer energy development and environmental stability.

2. Material and methods

2.1. Experimental apparatus

Considering that the hydrates are typical phase change materials, the conditions required for their stabilization and testing are more demanding than those for most energy minerals, *e.g.*, shale and coal. Conventional AFM cooling stages have limited cooling capacity, which is not ideal for maintaining hydrate stability. Therefore, in collaboration with Bruker Corporation and Instec Corporation, a Dimension Edge AFM has been modified to equip it with temperature control and dehumidification functions for experimental measurements of the hydrates in this study (Fig. 2). With the self-designed cold stage, the lowest temperature of the hydrate sample can be adjusted to 113.15 K with a precision of ±0.1 K. Moreover, the coolant circulation system of the cold stage was carefully optimized to minimize vibrations induced by liquid flow, ensuring that mechanical noise does not affect the force measurement accuracy. The central, round convex section of the cooling stage serves as the sample stage, with a diameter of 14 mm (Fig. 2(c)). Both the AFM and cooling stages were installed in an adiabatic and sealed glove box. Additionally, the glove box was filled with dry nitrogen gas and subsequently dried using a molecular sieve. In this manner, the dew point of air in the glove box

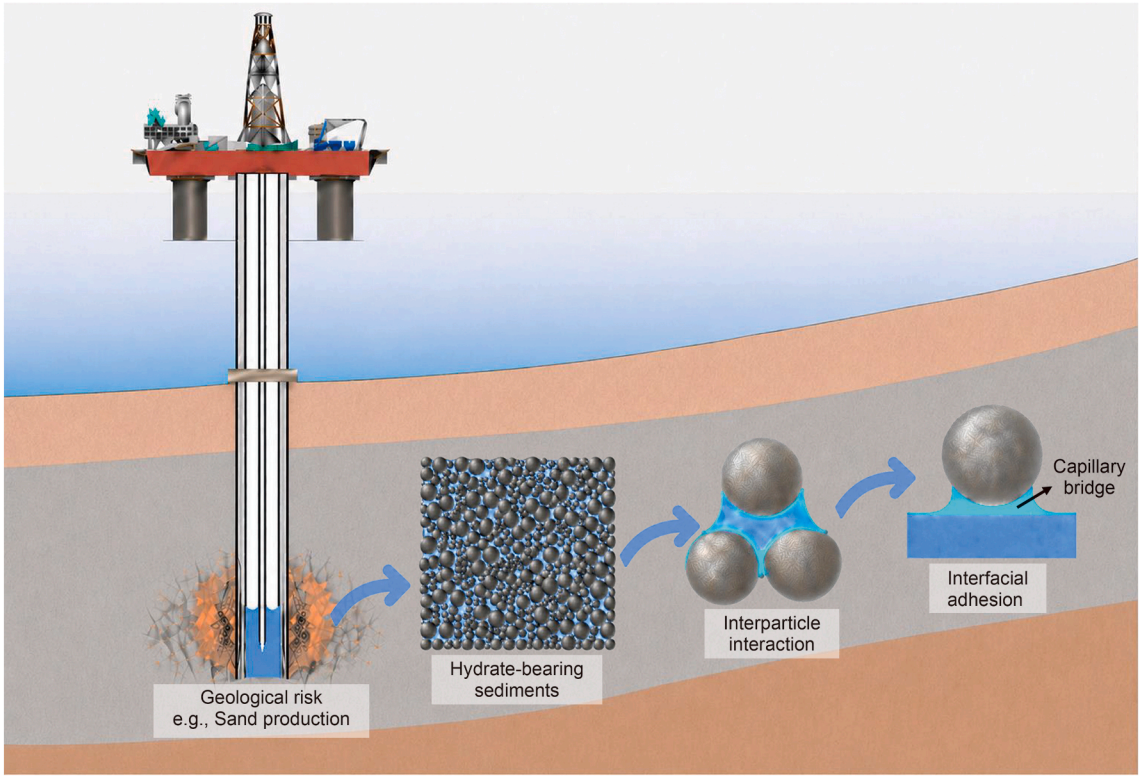


Fig. 1. Schematic illustration linking macroscale geological risk in hydrate-bearing sediments to microscale interfacial adhesion mediated by capillary bridge formation.

was maintained below 213.15 K in our study; hence, water condensation or ice formation under the experimental temperature (a minimum of 243.15 K) was prevented.

It should be noted that the current AFM system, like most commercial instruments, is designed for ambient pressure operation. The piezoelectric scanner, optical detection system, and cantilever are sensitive to pressure variations, making it challenging to maintain temperature stability and measurement accuracy at pressures exceeding the typical operating range of conventional AFM systems (Brand et al., 2018), particularly given that the pressure in natural hydrate reservoirs can exceed 10 MPa (Zhao et al., 2024). In addition, conducting measurements with flammable gases such as methane in the sealed glove box would raise safety concerns. In future work, in situ comparative validation experiments under elevated-pressure conditions will be treated as a priority, because the systematic introduction of pressure effects is expected to further enrich and test the interfacial mechanisms proposed in this study. As the pressure tolerance of such instruments improves, extending these measurements to high-pressure environments will therefore be an important next step for evaluating the pressure dependence of hydrate interfacial behavior and further validating the present mechanistic framework.

2.2. Preparation of hydrate samples

Clathrate THF hydrates were synthesized by cooling the 6.58 mol% THF (Shanghai Aladdin Biochemical Technology Co., Ltd.) solution from 278.15 K to 253.15 K, using THF hydrate as a proxy for natural gas hydrates (Lin et al., 2024). THF hydrate can form at atmospheric pressure and temperatures below 277.5 K, and is widely used as a proxy for natural gas hydrates (Li et al., 2023a; Luo et al., 2024; Xue et al., 2024) due to its mechanical properties similar to those of methane hydrate and its type II structure, commonly found in natural gas hydrates (Vlasic et al., 2019). The hydrate samples, prepared using the aforementioned process, exhibited a thickness of around 0.23 mm. Raman spectroscopy analysis confirmed that the hydrate samples, formed under the same conditions, were pure (Li et al., 2023a). Notably, although the mechanical properties of single hydrate crystals are anisotropic at the molecular scale (Wu et al., 2015), the hydrate samples formed in this study are polycrystalline, and their mechanical differences caused by crystal orientation were not observed in our experiments. Therefore, to simplify the discussion, the hydrate samples were considered isotropic.

2.3. Probe modification

We developed a micromanipulation-based technique to attach individual micrometer-sized mineral particles to tipless cantilevers, enabling direct investigation of interfacial adhesive behaviors between mineral microparticles and clathrate hydrates. This approach overcomes a limitation of conventional MMF measurements (Luo et al., 2024), which have difficulty assessing fine sediment particles in the micrometer to tens of micrometers range, thereby enabling measurements at a scale consistent with the particle size of natural hydrate reservoir sediments. Taking the modification of sediment particle probes as an example, the steps are as follows: (1) Sediment particles were selected from hydrate reservoirs in the South China Sea and washed with ethanol and ultrapure water. (2) The solution was deposited on a glass slide and allowed to dry. (3) Using a high-resolution optical microscope and a micromanipulation stage, an ACTA-type AFM probe (which lacks a tip and only has a cantilever) was positioned to contact the adhesive-coated cantilever. (4) The cantilever was then moved above the glass slide, and a single sediment particle was selected and fixed at the probe's tip.

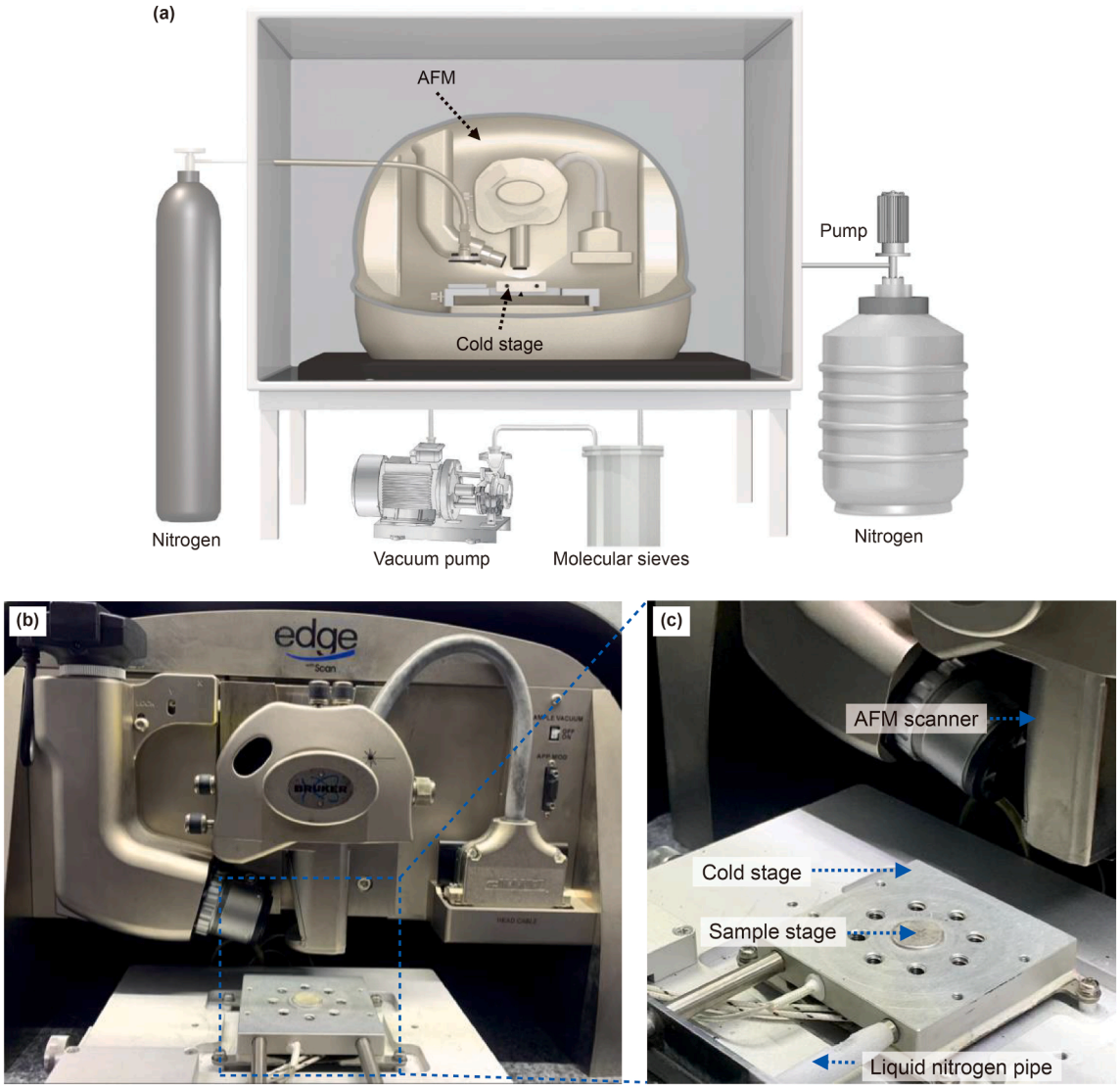


Fig. 2. Modified atomic force microscope system. **(a)** Schematic diagram adapted from Li et al. (2024); **(b)** core component photograph; **(c)** temperature control component photograph.

Using this method, hydrate sediment particles and silica (SiO_2) microspheres were successfully attached to the probe tips, as shown in Fig. 3. The particular descriptions and characteristics of the hydrate sediment particles can be found in our previous study (Wang et al., 2021). Various probes with SiO_2 microspheres, ranging in diameter from 5.0 μm to 19.8 μm, were fabricated (Fig. 3(b)–(f)), with the microspheres being hydrophilic. These microspheres are similar to the main chemical components and median particle sizes found in typical mud silty hydrate reservoirs. In fact, various parameters (such as size) of SiO_2 microspheres are easier to adjust for the comparative study of adhesion force owing to their similar spherical shapes, and sediment particles are used for comparison, which can promote our understanding of hydrate–sediment interactions in real hydrate reservoirs.

The elastic coefficients of the mineral probes were measured using the Sader method with AFM (Green et al., 2004). This method is suitable for obtaining elastic coefficients greater than 1 N/m for probes with rectangular cantilevers, and can ensure the accurate analysis of adhesion force. The measured probe elastic coefficients are presented in Table 1.

2.4. Experimental methods

Surface morphology test method. Our previous studies have confirmed that AFM tapping mode is suitable for measuring the three-dimensional morphology of hydrates (Li et al., 2023a, 2024). Similarly, in this study, the surface morphology of the hydrate was measured at 257.55 K using a commercial rectangular probe (OTESPA-R3, Bruker Corporation, with a radius of 3 nm) in AFM tapping mode. During morphological testing, the probe tip penetrated the liquid film on the hydrate surface, ultimately reaching the solid hydrate crystals (Li et al., 2024). This implies that the hydrate morphology represents the outermost layer of the solid hydrate surface without the influence of the liquid film (Li et al., 2024).

Analytical method. The interfacial interaction characteristics between the hydrates and mineral microparticle probes were obtained from force–distance curves using an AFM contact mode, as shown in Fig. 4. During the loading process, the microparticle approached (Process A), made contact (Process B) and then continuously pressed into the hydrate surface until reaching the

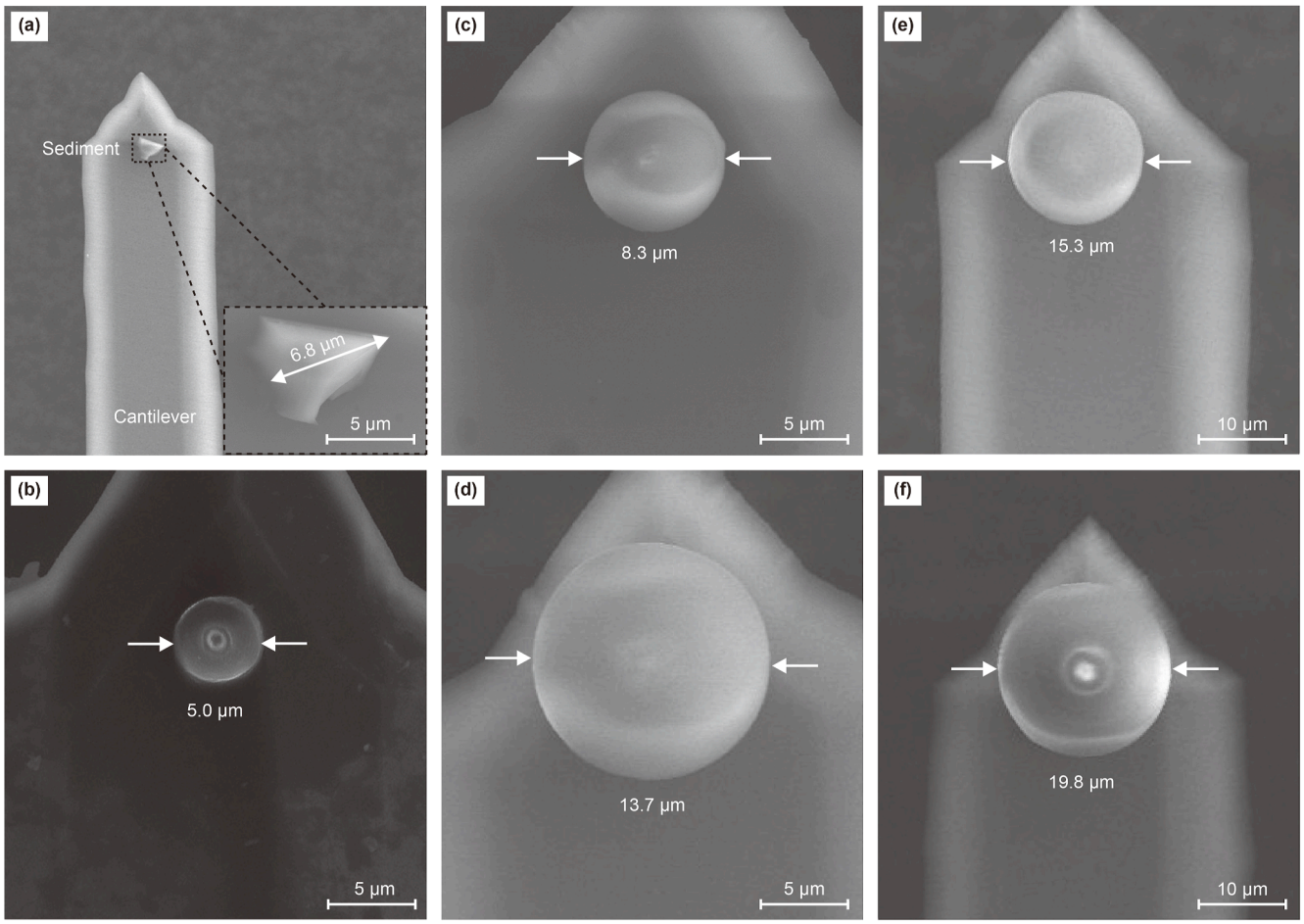


Fig. 3. Mineral microparticle probes measured using a scanning electron microscope (SEM). **(a)** An SEM image of a hydrate sediment microparticle probe; **(b)**–**(f)** SEM images of silica microsphere probes.

Table 1
Elastic coefficients of mineral microparticle probes.

Label in Fig. 3	(a)	(b)	(c)	(d)	(e)	(f)
Type	Sediment probe	SiO_2 probe	SiO_2 probe	SiO_2 probe	SiO_2 probe	SiO_2 probe
Elastic coefficient, N/m	27.6	36.46	31.29	29.65	28.98	27.5

preset load value (Process C). This preset load is referred to as the contact force in this study. After the preset contact force was applied to the hydrate surface, the position of the AFM scanner was held for a period, which was regarded as the contact time. Usually, the contact time was 0, which means unloading immediately upon reaching the preset load, as shown in Fig. 4.

The principle for calculating indentation depth is as follows: the movement distance Z_d of the AFM scanner during process B–C of Fig. 4 consists of two parts, the indentation depth of the microparticle probes into the hydrate surface and the deflection of the probe cantilever. The cantilever deflection can be obtained by dividing the measured force by the elastic coefficients of the microparticle probes (as shown in Table 1). Therefore, by subtracting the deflection of the cantilever from the total distance Z_d, the depth of mineral microparticle penetration into the hydrate surface, which is the indentation depth, can be calculated. During the unloading process (blue line in Fig. 4), the capillary bridge force between the mineral microparticle and the hydrate surface prevented their separation. When the pulling force produced by the cantilever deformation exceeded the capillary bridge force, the mineral microparticle detached from the hydrate surface with a sudden jump (Process D). In this case, the adhesion force was equal to the maximal pulling force (black dotted line in Fig. 4).

Unless otherwise specified, we used a SiO_2 microsphere probe with a diameter of 8.3 μm, and set the loading and unloading rates at 10 μm/s with a contact force of 4.36 μN, as the standard parameter settings to obtain the force–distance curves. These standard settings were used only as baseline conditions for force–distance measurements. In the corresponding sensitivity tests, surface morphology, contact force, temperature, contact time, loading/unloading rate and microsphere size were systematically varied to evaluate their effects on the measured adhesion force.

3. Results

3.1. Effects of surface morphology on hydrate adhesion

Surface morphology of THF hydrate was investigated as shown in Fig. 5(a) for the visual identification of hydrates. The results revealed that THF hydrate growth at the gas–liquid interface

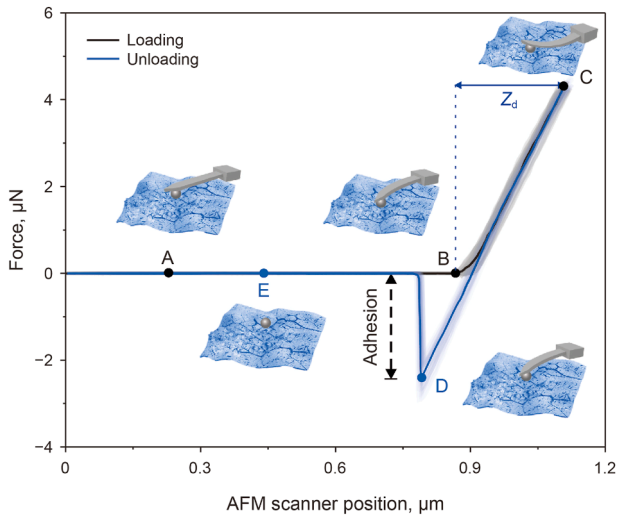


Fig. 4. Force–distance curve between the hydrate and the mineral microparticle probe.

formed a polycrystalline compound consisting of multiple hydrate grains. These grains are predominantly elliptical or polygonal, with diameters ranging from approximately 1.5 μm to 20 μm. To investigate the impact of hydrate surface morphology on adhesion force measurement, we extracted the line profile of the hydrate surface, as indicated by the dotted line in Fig. 5(a). This profile was represented by the blue line in Fig. 5(b), illustrating the height fluctuations of the hydrate surface. In contrast to the flat positions on the hydrate surface, the concave hydrate surface increased the capillary liquid bridge width relative to the mineral microparticle due to a larger number of contact points (Phan et al., 2022). This effect is further amplified by the fact that the liquid film on the hydrate surface exhibits flowability, whereby the liquid tends to migrate from higher to lower positions. Consequently, the concave regions, which are lower in height, accumulate a thicker liquid film, leading to an increase in capillary bridge thickness, while convex surfaces have the opposite effect, with the liquid film tending to be thinner in these elevated areas (Li et al., 2024). Therefore, the undulating hydrate surface led to slight differences in the adhesion force, even under the same experimental conditions. This factor is also of practical relevance, because local surface roughness and topographic heterogeneity in hydrate reservoirs can directly alter capillary bridge geometry and thereby influence the dispersion and magnitude of interfacial adhesion.

To minimize this uncertainty, the adhesion force was represented by the statistical data of 40 independent tests. It is worth noting that, during repeated testing, the mineral particles would randomly reposition on the hydrate surface after each independent experiment to avoid multiple compressions at the same position on the hydrate surface. The distribution of adhesion forces is illustrated in Fig. 5(c)–(e) as an example. In general, they are close to a normal distribution. It should be noted that the spread in Fig. 5(c)–(e) may reflect statistical scatter arising from local surface heterogeneity and random contact positions, rather than instrumental measurement error of the AFM system. This indicates that the influence of hydrate surface morphology on the adhesion force between hydrate and mineral particles is statistically negligible, based on the 40 repeated tests in this study.

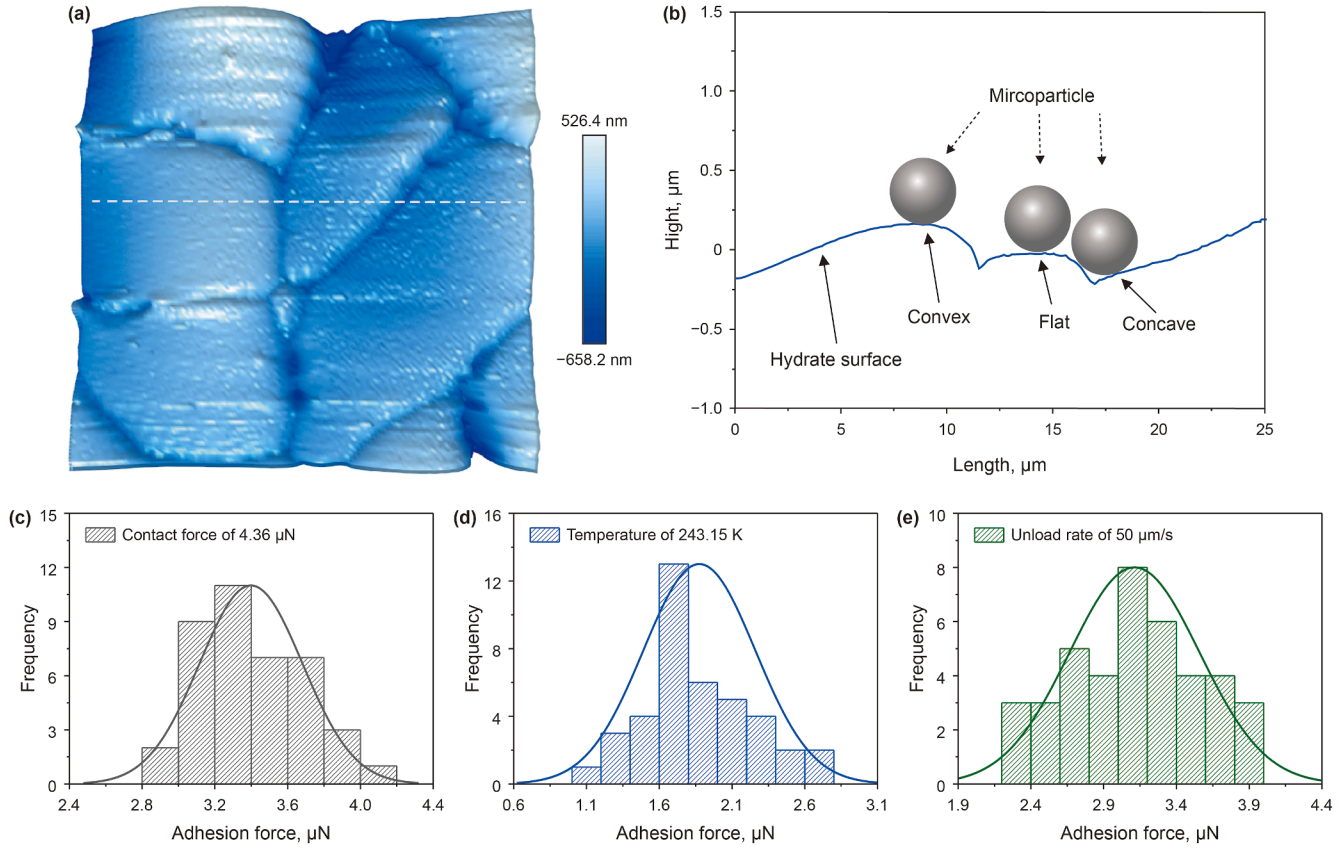


Fig. 5. Surface characterization of THF hydrate. **(a)** Surface morphology of the hydrate measured at 257.55 K. The scanning range is 25 μm × 25 μm. **(b)** Schematic of the effects of surface morphology on adhesion force. **(c)**–**(e)** Data distributions of adhesion forces.

Therefore, the mean adhesion force from 40 independent measurements was used in the subsequent analyses to minimize the influence of local morphological variability.

3.2. Effects of contact force on hydrate adhesion

The evolution of adhesion forces between the hydrate surfaces and the sediment microparticle as well as the SiO_2 microsphere at various contact forces is shown in Fig. 6(a). The results demonstrated that the average adhesion forces of the SiO_2 microsphere to the hydrate were slightly larger than those of the sediment particle under the same experimental conditions. Under the contact forces ranging from 0.727 μN to 7.27 μN, the average adhesion forces of the SiO_2 microsphere and the sediment microparticle to hydrate surfaces were 2.07–3.72 μN and 0.63–2.43 μN, respectively. This slight difference in adhesion force may be due to differences in the size and surface roughness between the sediment microparticles and the SiO_2 microsphere (Fig. 3). Nevertheless, the adhesion forces measured using these two mineral particles were of the same order of magnitude and always increased with increasing contact force, which agrees with the previous studies (Hu and Koh, 2017; Luo et al., 2024).

The evolution of the adhesion force with indentation depth, as shown in Fig. 6(b), reveals a generally linear relationship. However, an unexpectedly high adhesion force, deviating from this linear trend, is observed at greater indentation depths, as indicated by the blue circle in Fig. 6(b), when the contact force reaches 7.27 μN. This deviation can primarily be attributed to the increase in both the indentation depth and the resulting contact area between the hydrate and the microparticles (Wang et al., 2020). Additionally, the applied contact force induces local melting (Cao et al., 2021), which further influences the adhesion force. As demonstrated by Li et al. (2026b), nanoindentation can induce local melting of the hydrate near the probe, leading to the formation of decomposition liquid on the hydrate surface. This suggests that, under the influence of contact forces, elastic and plastic deformations, along with possible decomposition, may occur simultaneously on the hydrate surface, further altering the mechanical interactions between the hydrate and mineral microparticles (Wu et al., 2015; Li et al., 2026b). The observed higher adhesion force at 7.27 μN, compared to the fitted value in Fig. 6(b), may thus be explained by stress-induced structural disruption (often referred to as stress-induced melting) (Li et al., 2026b). Consequently, under high contact forces, this mechanical breakdown locally disrupts the hydrate clathrate structure, thickening the capillary bridge and leading to a significant increase in the adhesion force.

3.3. Effects of temperature on hydrate adhesion

Fig. 7 indicates that the adhesion force increased exponentially from 1.11 μN to 5.17 μN with temperature rising from 227.55 K to 267.55 K, a trend consistent with reported adhesion behaviors of various clathrate hydrates (Luo et al., 2024). To explore the mechanism underlying the temperature effect, the indentation depths at different temperatures were calculated (blue portion in Fig. 7). The indentation depth showed an overall linear growth tendency (blue trendline) with the temperature increasing, while it was obviously inconsistent with the trend of hydrate adhesion force (black trendline). This finding suggested that, under different temperature conditions, although the increased indentation depth may widen the contact area and the capillary bridge between the mineral microsphere and the hydrate, its contribution to adhesion enhancement remained limited.

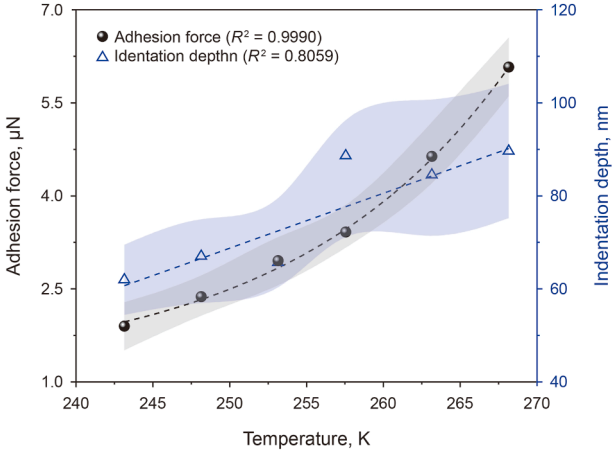


Fig. 7. Effect of temperature on adhesion forces and indentation depth. Contact force was maintained at 4.36 μN.

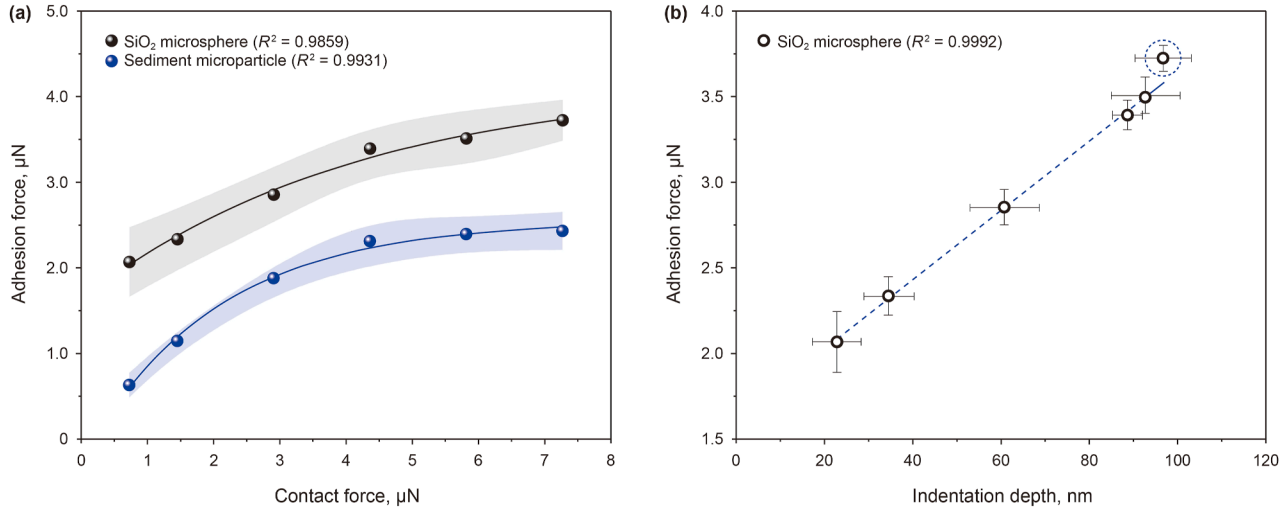


Fig. 6. Trend of adhesion force with contact force and indentation depth. **(a)** Adhesion forces measured at different contact forces. The temperature was maintained at 257.55 K. Error bars represent the standard deviation of the adhesion force data. **(b)** Adhesion force as a function of indentation depth. The dotted line in (b) represents the fit to the first five data points, while the solid line is the extended trend, used to highlight the deviation in measurement results at higher contact forces.

Based on the temperature dependence of adhesion force, Nguyen et al. (2021, 2022) proposed a microscopic mechanism in which adhesion is induced by the assumed existence of a nanometer-thick quasi-liquid layer (QLL) on hydrate surfaces. From an engineering perspective, this temperature dependence is particularly important because temperature variations in hydrate reservoirs directly influence hydrate stability and interfacial adhesion through the evolution of the surface liquid layer. Recently, we further advanced this line of work and successfully measured the QLL thickness and structure of hydrates at various temperatures (Li et al., 2023a, 2024). The quantitatively determined QLL thickness provides a crucial baseline parameter for characterizing the liquid layer at the hydrate surface, which directly influences capillary bridge formation and adhesion behavior. Therefore, based on the adhesion force data in Fig. 7 and the QLL thickness data for THF hydrate obtained in our prior work at the same temperature using the same AFM system and under identical conditions (Li et al., 2023a), the quantitative relationship between them could be established, as shown in Fig. 8. The results revealed that the adhesion force increased linearly with the QLL thickness. This indicates that the thickening of the hydrate QLL at higher temperatures was the primary reason for the increase in adhesion force between the hydrate and mineral microparticles (Nguyen et al., 2021; Li et al., 2023a).

3.4. Effects of contact time on hydrate adhesion

As shown in Fig. 9, the influence of contact time on adhesion can be divided into two stages. During the period from 0 to 0.375 s, the increasing tendency of the adhesion forces with contact time might be related to three factors: (1) Under a persistent contact force, the microparticle probe is continuously pressed into the hydrate surface. A longer contact time increased the contact area between the mineral microparticle and the hydrate, which improved the adhesion force. (2) The degree of hydrate melting under the applied load may also be intensified (Li et al., 2026b). Therefore, the increased contact time introduced more liquid by hydrate decomposition to strengthen the capillary bridge and adhesion force. (3) According to the dynamic meniscus model, as contact time increases, the viscosity of the liquid film in the contact zone may increase under the combined effects of Laplace pressure and exclusion pressure (Lai and Meng, 2018). In essence, all three contributions—mechanical indentation, thermally-driven melting, and a pressure-induced viscosity increase of the liquid bridge—may collectively contribute to the time-dependent strengthening of adhesion at the interface.

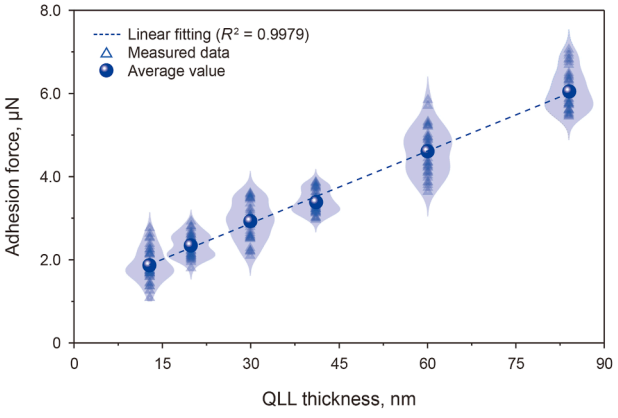


Fig. 8. Relationship between the adhesion force and the QLL thickness on the hydrate surface.

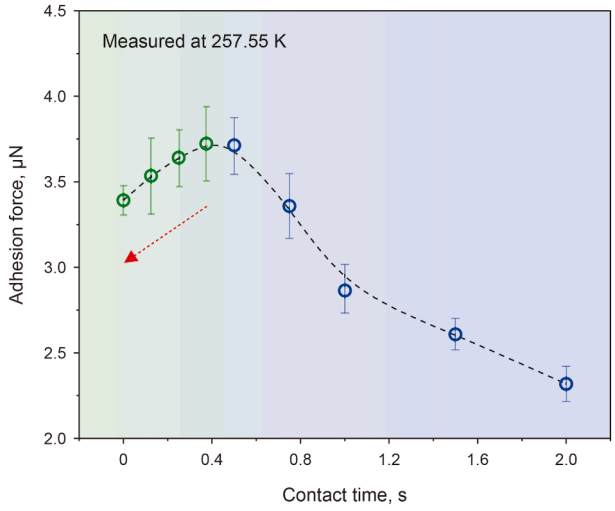


Fig. 9. Effect of contact time on adhesion forces between the SiO_2 microsphere and the hydrate. Both the loading and unloading rates were 10 μm/s, with a contact force of 4.36 μN and a temperature of 257.55 K.

With prolonged contact times between 0.5 s and 2 s, the observed decrease in adhesion force may be related to the secondary formation of hydrate or ice. Our previous work suggested that THF tends to adsorb onto the outermost layer of the quasi-liquid film on the hydrate surface (Li et al., 2024). Considering the concentration gradient, some of the THF may diffuse out of the surface film, leading to the secondary formation of partial hydrate or ice at the test temperature of 257.55 K (below the phase equilibrium temperature of 277.5 K). This recrystallization process can contribute to the thinning of the capillary bridge and the weakening of the adhesion force. Additionally, as the contact time increases, the liquid produced during pressing tends to transition toward a solid phase, further diminishing the adhesion force. We note, however, that redistribution or thinning of the capillary bridge, changes in the effective contact geometry, and time-dependent mechanical relaxation at the interface may also contribute to this non-monotonic evolution of adhesion force (Lai et al., 2022; Luo et al., 2024). The present adhesion-force data alone do not allow the relative contributions of these concurrent processes to be unequivocally separated. Consistent with these combined effects, at a contact time of 2 s, the adhesion force is lower than at 0 s.

This non-monotonic evolution, with an initial increase followed by a decrease, contrasts with previous studies over longer time scales (up to 10^5 s), which reported a monotonic increase in hydrate adhesion with contact time (Hu and Koh, 2017; Liu et al., 2023). The behavior observed at short contact times highlights the significance of investigating interfacial dynamics on the micro/nano scale. The high temporal and spatial resolution of our cryogenic AFM system enabled us to resolve this non-monotonic short-time adhesion response. Such behavior may reflect the combined influence of several interfacial processes, including hydrate decomposition, possible recrystallization or solidification of the interfacial liquid, liquid bridge redistribution, and interfacial mechanical relaxation. This highlights the complexity of hydrate adhesion at short times and suggests that multiple mechanisms may operate in parallel. To gain deeper insight into these phenomena, further studies combining experimental observations with numerical simulations are needed to visualize and quantify the evolution of interfacial interactions between mineral microparticles and hydrates. This will contribute to a better

understanding of hydrate plastic deformation and decomposition, and of the macroscopic mechanical degradation of hydrate reservoirs.

3.5. Effects of loading rate and unloading rate on hydrate adhesion

To elucidate the rate-dependent evolution of interfacial adhesion behavior and its underlying microscopic mechanisms between the mineral microparticles and the hydrates, adhesion forces were systematically investigated under varying loading/unloading rates (Fig. 10). Overall, the changing tendency of adhesion forces can be divided into two parts. At lower rates (1–10 μm/s), the adhesion generally increased, with the unloading rate (blue line) being more effective in enhancing adhesion than the loading rate (black line).

Conversely, at higher rates (15–50 μm/s), the loading rate became the dominant factor in reducing adhesion, while the influence of the unloading rate was negligible. This transition is attributed to the decrease in compression time—the duration from the initial contact of the microspheres with the hydrate surface until the preset contact force is reached—as the loading rate increases. Critically, when the loading rate exceeded 10 μm/s, the compression time became shorter than the minimum duration required for adhesion development, as inferred from the data at zero contact time in Fig. 10. It is important to note that a contact time of zero does not imply zero compression time, as these are defined differently. In this study, the contact time refers to the duration during which the AFM cantilever and the probe's rigid substrate remain stationary after the preset load is applied. Thus, the observed adhesion reduction at high loading rates (Fig. 10) results directly from the shortened compression time, as indicated by the red arrow in Fig. 10.

3.6. Effects of microsphere size on hydrate adhesion

We directly measured the interfacial adhesion forces between hydrate surfaces and SiO_2 microspheres, with radii ranging from 2.5 μm to 9.9 μm, which are comparable to the particle sizes of fine-grained hydrate sediments in marine environments (Fig. 11). The results showed that the adhesion force increased approximately linearly with increasing microsphere radius under the same contact force and temperature. To compare the tendency of adhesion force F_c measured by the microspheres of different sizes, F_c was divided by the microsphere radius and denoted as the force F^* (blue portion in Fig. 11). This demonstrated that F^* decreased with increasing microsphere radii, which was similar to the behavior of cyclopentane hydrate particles in the liquid phase (Wang et al., 2020). This size range is of direct reservoir relevance, because hydrate-bearing sediments are predominantly composed of particles in the micrometer to tens-of-micrometer range, and the contact mechanics at this scale strongly affect interfacial adhesion.

This trend implies that the contact area between the particle and the hydrate surface does not increase linearly with the radius, likely due to a transition in the dominant deformation mechanism. For smaller particles, localized plastic deformation may be more pronounced. The stress-induced melting, which causes localized melting and the release of fluid, may also be more pronounced. This process leads to an increase in adhesion force F^* (Li et al., 2026b). In contrast, larger particles may undergo less plastic deformation and instead form a more elastic or heterogeneous contact with the hydrate surface. The lack of significant stress-induced melting leads to a reduced extent of the hydrate decomposition, and to less liquid phase formation at the interface. As a result, the adhesion force F^* decreases.

4. Discussion

The experimental results presented in Section 3 confirm that the hydrate exhibits non-ideal elastomeric behavior and is susceptible to plastic deformation, particularly under elevated contact forces. Consequently, conventional elastic theories commonly used to describe adhesive interactions—such as the Johnson-Kendall-Roberts (JKR) contact model—may be of limited applicability in analyzing hydrate samples. Prior research has consistently demonstrated that adhesion in such systems is predominantly governed by capillary bridge formation (Aman and Koh, 2016; Wang et al., 2022a, 2022b).

In line with this, our findings show that various experimental parameters modulate the adhesion force by modifying the liquid layer present on the hydrate surface, which is critical for capillary bridge development. Specifically, increasing the temperature promotes the growth of a QLL through crystal premelting, thereby enhancing the thickness of the capillary bridge and the adhesion. Higher contact forces, in turn, induce mechanical disruption of the hydrate lattice, generating decomposition liquid that further thickens the surface liquid layer and reinforces the capillary bridge.

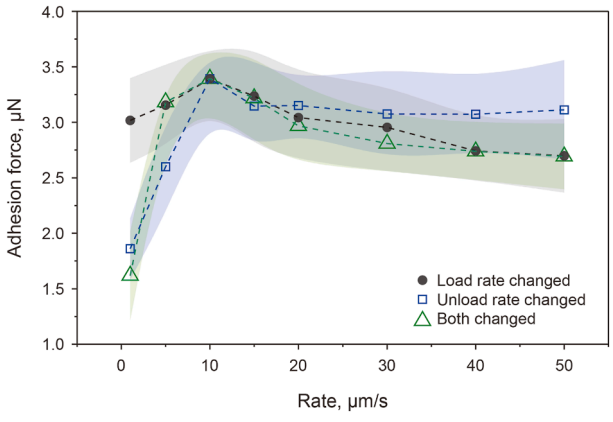


Fig. 10. Changing tendency of adhesion forces between the SiO_2 microsphere and the hydrates with various loading and unloading rates. The contact force was maintained at 4.36 μN, and the test temperature was 257.55 K.

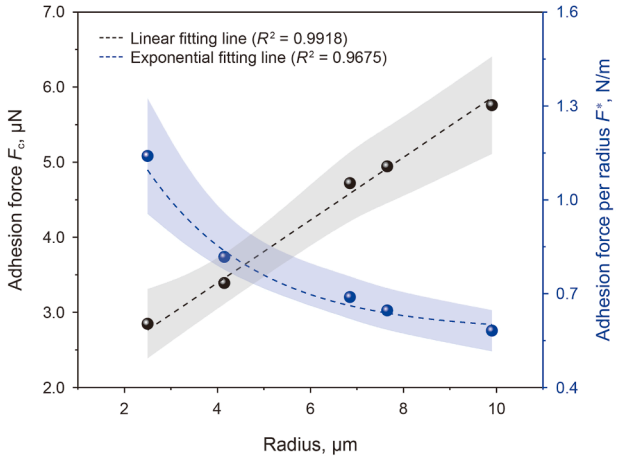


Fig. 11. Relationship between adhesion force and microsphere radius. The contact force was maintained at 4.36 μN, and the test temperature was 257.55 K.

Additionally, variations in the loading rate influence the coupled mechanical response of the liquid layer—comprising both the QLL and decomposition liquid—and the underlying hydrate solid framework, thereby regulating the formation and rupture dynamics of the capillary bridge. Although contact force, contact time, and loading/unloading rate are instrument-controlled inputs in AFM measurements, they represent the local stress state and contact kinetics at the particle–hydrate interface. Their systematic variation is therefore essential for linking experimentally controlled conditions to the micromechanical mechanisms governing adhesion. Therefore, it is necessary to establish an accurate liquid bridge model to help comprehensively characterize the adhesion behaviors at the hydrate–mineral interface.

4.1. Capillary bridge model for microparticle-plate hydrate system

Given the pivotal role of the surface liquid layer in controlling adhesion, we propose a modified model that simultaneously incorporates the contributions of the QLL and the plastic deformation behavior of the hydrate. This unified framework provides a comprehensive explanation for the observed adhesion forces. In this model, the capillary bridge is formed between the hydrate surface and the microparticle by the combined presence of the QLL and any decomposition liquid (Gelman Constantin et al., 2018; Nguyen et al., 2022; Li et al., 2023a). The maximum pull-off force, defined as the adhesion force F_c, comprises two components: the surface tension contribution F_s acting along the three-phase contact line on the microparticle, and the Laplace pressure force F_p arising from the curvature of the liquid bridge (Fig. 12).

To simplify the derivation of the capillary bridge model, spherical microparticles of radius R were employed. The Laplace pressure force is characterized by defining the principal radii of curvature of the liquid bridge: r_1 in the vertical plane and r_2 in the horizontal plane. Denoting the liquid-vapor surface tension of the THF hydrate system as γ_{lv}, the Laplace pressure difference ΔP across the liquid-vapor interface is expressed as (Butt and Kappl, 2009):

$$\Delta P = \gamma_{lv}\left(\frac{1}{r_1}+\frac{1}{r_2}\right) \tag{1}$$

Because the radius of the microparticle was far greater than the thickness of the QLL, the radius of curvature r_2 was approximately equal to $R\sin\varphi$, where φ represents the embracing angle of the three-phase wetting line on the microparticle. Prior research has confirmed that the hydrate is highly hydrophilic, and the QLL can completely spread on the hydrate surface (i.e., the contact angle of QLL on the hydrate surface approaches zero) (Lin et al., 2023). With these assumptions, the principal curvature radius r_1 can be approximated by the following relationship (Butt and Kappl, 2009), modified from the classical capillary bridge theory:

$$\frac{1}{r_1} \approx \frac{1+\cos(\varphi+\theta)}{R(1-\cos\varphi)+(d+h)} \tag{2}$$

where θ represents the contact angle between the QLL and the mineral microparticle; d represents the distance between the bottom of the mineral microparticle and the QLL when the capillary bridge is broken. The equation considers the liquid film and the solid hydrate surface as two independent entities, thus accounting for the influence of the thickness of the liquid film (h) on the hydrate surface. It is important to note that h refers to the liquid film thickness on the hydrate surface resulting from the interaction with the microparticle, which is composed of both the QLL and the potential decomposition liquid formed during the indentation process. Under certain conditions, as shown in Fig. 12(b), when the probe is unloaded and the microparticle detaches from the hydrate surface, the liquid film between the hydrate and the microparticle is stretched, exceeding the QLL thickness on the hydrate surface (h_0).

The physical meaning of $(d + h)$ in Eq. (2) is the distance between the microparticle bottom and the original solid hydrate surface. When the hydrate is compressed by the mineral microparticle, both elastic and plastic deformations may occur simultaneously, causing d to become negative. For convenience, distances above the hydrate surface are considered positive, while those below the surface are negative. Consequently, two distinct scenarios are anticipated: first, as shown in Fig. 12(a), the capillary bridge breaks above the hydrate surface when $(d + h) > 0$; second, when the probe is pressed into the hydrate, the break occurs at $(d + h) < 0$, as shown in Fig. 12(b).

Based on previous reports (Butt and Kappl, 2009; Harrison et al., 2015), the equation for calculating the adhesion force can be summarized as follows:

$$F_c = F_P + F_s = \pi R^2 \sin^2\varphi\cdot\Delta P + 2\pi R\gamma_{lv}\sin\varphi\sin(\varphi+\theta) \tag{3}$$

Combining Eqs. (1)–(3), F_c was finally characterized using Eq. (4):

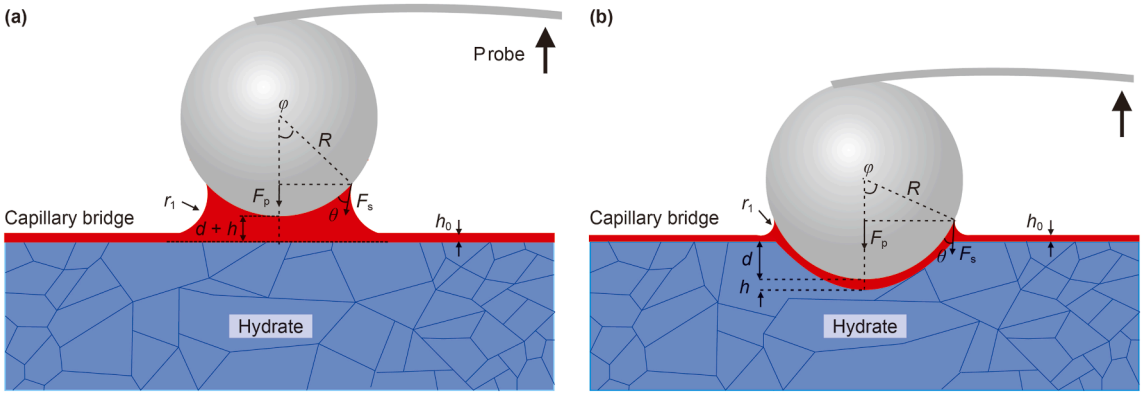


Fig. 12. Model of a capillary bridge between the mineral microparticle and the hydrate surface. **(a)** Capillary bridge break occurring above the hydrate surface; **(b)** capillary bridge break occurring below the hydrate surface.

$$F_c = \pi R^2 \sin^2 \varphi \gamma_{lv} \left(\frac{1 + \cos(\varphi + \theta)}{R(1 - \cos\varphi) + (d + h)} + \frac{1}{R \sin\varphi} \right) + 2\pi R \gamma_{lv} \sin\varphi \sin(\varphi + \theta) \quad (4)$$

In contrast to the typical capillary bridge theory, this improved model, named the QLL-deformation capillary bridge model, takes into account the QLL thickness and the plastic deformation of the hydrate surface under loading. As a result, it establishes a quantitative relationship between the surface structural characteristics and the mechanical properties of hydrates. In the actual mud silt hydrate reservoir, where the median particle size of sediment particles is approximately 10 μm (Wang et al., 2021), this improved capillary bridge model can facilitate the accurate assessment of adhesive behavior between hydrates and sediments at micro–nano scales.

Consider the SiO_2 microsphere probe with a radius R of 4.15 μm as an example. The θ between the SiO_2 microspheres and the water film was 30–72°, with an average value of $\theta = 51°$ (Corona-Arroyo et al., 2018). For simplicity, we assumed that the surface tension of the liquid on THF hydrate γ_{lv} was equal to the surface tension of the THF solution, which was measured to be approximately 0.067 N/m using an automatic surface tensiometer (Shanghai FangRui instrument Co., Ltd, China). Based on the aforementioned assumptions, the theoretical adhesion force is related to the parameters φ and the distance $(d + h)$ according to the QLL-deformation capillary bridge model.

4.2. Plastic deformation of THF hydrate

Identifying the plastic deformation behavior of the hydrate when it is squeezed by microparticles is crucial for understanding the mechanism of adhesion behavior, especially on the micro- and nano-scale. The change in adhesion force between the hydrate and the microsphere with distance $(d + h)$ was calculated, as shown in Fig. 13. The results showed that the theoretically calculated relationship between adhesion force and distance $(d + h)$ was hyperbolic, of which two asymptote lines were $F_c = 0$ and $(d + h) = R(\cos\varphi - 1)$. When the theoretical value of the adhesion force was compared to the measurement data at the higher contact force, such as the adhesion force of 3.725 μN at the contact force of 7.273 μN, the theoretical values were consistent with the experimental results only if the distance $(d + h) < 0$. This indicates that the distance $(d + h)$ could be negative, and the hydrate surface underwent plastic deformation and did not fully recover before the capillary bridge ruptured, leaving the probe tip below the original surface level, as shown in Fig. 12(b).

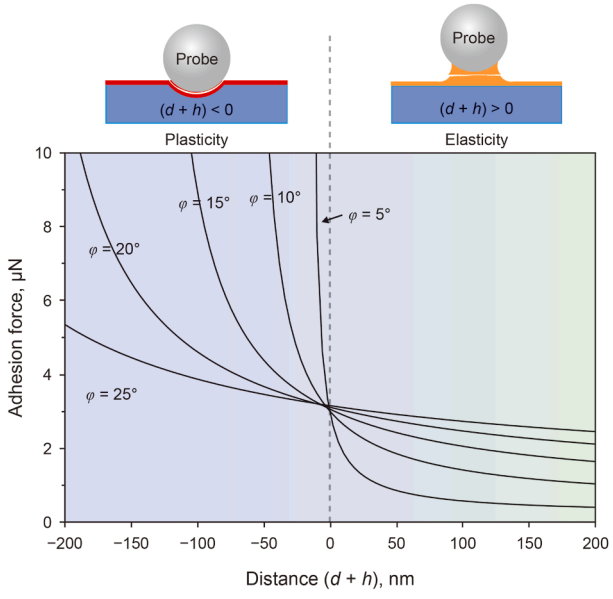


Fig. 13. Theoretical curves of adhesion force calculated using the modified capillary bridge model.

The theoretical adhesion force exhibited an increasing tendency when the distance $(d + h)$ decreased in Fig. 13, while the measured adhesion force increased as the contact force increased in Fig. 6(a). This correlation can be attributed to the augmented contact force inducing greater indentation depth, thereby reducing the distance $(d + h)$. Furthermore, under the low-temperature experimental conditions, the partial decomposition liquid of the hydrate might transform into a solid phase within moderate timescales. Consequently, the capillary bridge between the hydrate and the microsphere was unable to fill the plastic deformation area of the hydrate surface, leading to the manifestation of negative $(d + h)$ values accompanied by a progressive increase in their absolute magnitudes. These observations confirm that plastic deformation occurred on the hydrate surface when subjected to compression, particularly at higher applied forces.

4.3. Influence of indentation depth and contact area on adhesion force

The dynamic stretching and deformation of the liquid bridge during unloading have a minimal impact on the adhesion force, since this force is defined as the maximum tensile force determined by the interaction between the hydrate and the microsphere at the moment of bridge rupture. However, our previous study (Li et al., 2023a) indicated that the QLL on the THF hydrate surface is relatively thin, on the order of tens of nanometers. To the best of our knowledge, directly observing the deformation of this nano-scale QLL at the moment of liquid bridge rupture remains a significant challenge. Therefore, we performed optical microscope observations to further investigate the deformation behavior of the liquid bridge between the particle–surface geometries, as illustrated in Fig. 14. The quantitative results from the macroscopic liquid bridge deformation experiments offer useful insights for predicting the behavior of micro-scale liquid bridges under similar conditions.

The preparation of THF hydrate particles for the macroscopic optical tests followed the method described in Section 2.2. In brief, two glass cantilevers were used, with the upper cantilever coated with a 6.58 mol% THF solution. The temperature was then decreased from 278.15 K to 243.15 K at a rate of 10 K/min and maintained at 243.15 K for 30 min to allow the solution to convert into hydrate particles. The hydrate particle was then moved down at a speed of 10 μm/s. After the hydrate particle contacted the liquid drop, the upper glass cantilever was raised until the liquid bridge between the hydrate particle and the lower glass cantilever broke. Due to the short contact time, the phase transition of the liquid drop was ignored. According to the deformation of the liquid bridge in Fig. 14, the tensile coefficient A of the liquid bridge between the top of the lower glass cantilever and the contact (or compression) bottom of the hydrate particle was calculated to be 1.13, 1.20, 1.16 and 1.16 (e.g., 831.8 μm/735.6 μm in Fig. 14(a) and (e)), with an average value of approximately 1.16. Similarly, the total tensile coefficient B of the entire liquid bridge deformation was calculated as 1.56, 1.50, 1.50, and 1.53 (e.g., 1020 μm/678 μm in Fig. 14(g) and (h)), with an average value of approximately 1.52.

To simplify the calculation, the variation of the capillary liquid bridge between the hydrate and the AFM mineral microsphere

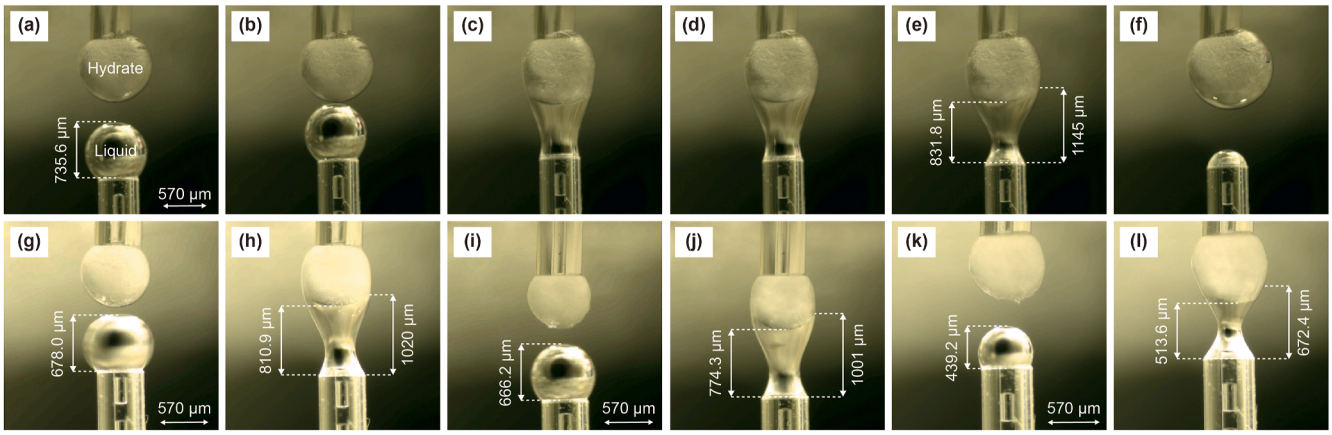


Fig. 14. Variation of liquid bridge observed by an optical microscope. **(a)–(f)** Complete deformation processes of the liquid bridge; **(g)–(l)** comparison of liquid bridges before and after deformation for different hydrate sizes. Each pair of adjacent images in (g)–(l) represents the liquid bridge before deformation and at the moment of bridge rupture.

probe (hydrate–solid surface systems) in this study is assumed to be analogous to that shown in Fig. 14. The schematic of the geometric relationship between the distance $(d + h)$ and φ is shown in Fig. 15. The plastic deformation depth of the hydrate when the capillary liquid bridge broke is D_{de}, and the equation is given as follows:

$$D_{de} = C \times D_{in} \tag{5}$$

where D_{in} is the indentation depth; C is the coefficient to evaluate the ratio between the hydrate plastic deformation and indentation depth. The value of C can reflect the proportion of elastic deformation and plastic deformation of the hydrate. For example, if C is zero, it means that the deformation of the hydrate surface completely recovered after unloading and the hydrate exhibits pure elasticity. If C is equal to 100%, it means that the deformation of the hydrate surface does not recover at all and that the hydrate exhibits purely plastic behavior.

The value of the parameter $(d + h)$ is closely related to parameter D_{de} and the deformation of the capillary bridge. Thus, according to the geometric relation in Fig. 15, the values of $(d + h)$ and φ can be calculated using Eqs. (6) and (7):

$$(d + h) = h_s – D_{de} = h_s – C \times D_{in} \tag{6}$$

$$\varphi = \cos^{-1}[(R + h_s - h_{lb} - C \times D_{in}) / R] \tag{7}$$

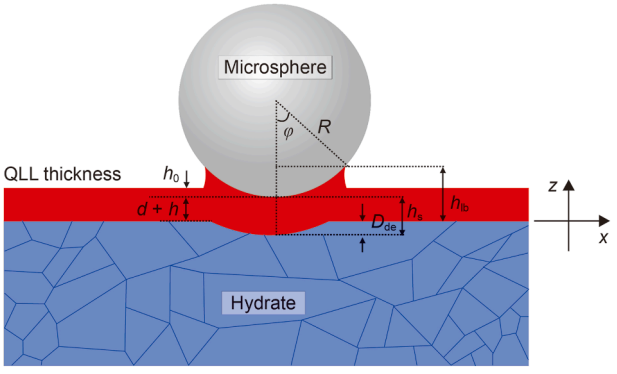


Fig. 15. Schematic of geometric relationship of QLL-deformation capillary bridge model parameters.

where the capillary liquid bridge thickness between the bottom of the microsphere and the upper surface of the solid hydrate after indentation is denoted as h_s, and the maximum tensile thickness of the capillary liquid bridge during probe withdrawal from the hydrate surface is denoted as h_{lb}.

As discussed in Section 4.1, the known parameters in the QLL-deformation capillary bridge model (Eq. (4)) include the radius R, surface tension γ_{lv} and contact angle θ, while the unknown parameters are the distance $(d + h)$, the embracing angle φ and the adhesion force F_c. The $(d + h)$ and φ are related to the h_s, h_{lb} and D_{in}, as described by Eqs. (6) and (7). When studying the effect of load, the experimental temperature was maintained at 257.55 K, and the QLL thickness on the THF hydrate surface h_0 before stretching was approximately 41.09 nm, according to our previous research (Li et al., 2023a). Under these conditions, h_s is calculated as $A \times h_0 = 47.66$ nm, and the h_{lb} is calculated as $B \times h_0 = 62.46$ nm, with the D_{in} given by Fig. 6. Thus, when the coefficient C is between 0 and 1, the theoretical adhesion forces are calculated using the QLL-deformation capillary bridge model (Eqs. (4)–(7)). These values are then compared with the experimental adhesion forces measured by AFM (Table 2). The average relative error represents the mean of the relative errors between the theoretical and experimental adhesion forces at the same contact force.

As shown in Table 2, when the plastic deformation depth of hydrate was 67.5% of the indentation depth (C = 67.5%), the theoretical adhesion forces had a good overall agreement with the measured adhesion forces. The parameters of the QLL-deformation capillary bridge model are shown in Table 3. This means that when the microspheres were pressed into the hydrate surface, the hydrate could undergo elastic and plastic deformation at the same time. The results of Table 2 also indicated that the theoretical adhesion forces were consistent with the measured values at higher contact forces, while the theoretical values of adhesion force were slightly smaller at the lower contact forces. However, if the plastic deformation depth of hydrate is equal to the indentation depth (C = 100%) at the lower contact force (e.g., contact force of 0.727 μN), the theoretical adhesion force is generally consistent with the measured value. We speculate that the mechanical properties of the solid hydrate near the QLL–hydrate interface may be weak. Thus, when the contact force was lower, this mechanical weakening effect of the QLL would be more remarkable because the indentation is shallow, and the ratio of the hydrate plastic deformation depth may be higher than 67.5% and even reach 100%.

Table 2
Comparison of measured adhesion forces and theoretical adhesion forces at different coefficient *C*.

Contact force, μN	0.727	1.455	2.909	4.364	5.818	7.273	Average relative error, %
Measured adhesion force, μN	2.068	2.336	2.855	3.393	3.51	3.725	—
Adhesion force (C = 100%), μN	1.909	2.426	3.534	4.66	4.818	4.986	23.96
Adhesion force (C = 80%), μN	1.702	2.123	3.027	3.952	4.083	4.213	13.12
Adhesion force (C = 70%), μN	1.598	1.969	2.77	3.591	3.707	3.823	9.249
Adhesion force (C = 67.5%), μN	1.572	1.93	2.705	3.499	3.612	3.724	8.779
Adhesion force (C = 65%), μN	1.546	1.892	2.639	3.408	3.516	3.625	9.185
Adhesion force (C = 62.5%), μN	1.519	1.853	2.574	3.315	3.42	3.526	11.21
Adhesion force (C = 60%), μN	1.493	1.814	2.508	3.223	3.324	3.426	13.44
Adhesion force (C = 0%), μN	0.841	0.841	0.841	0.841	0.841	0.841	70.43

Table 3
Optimal parameters of QLL-deformation capillary bridge model.

Contact force, μN	0.727	1.455	2.909	4.364	5.818	7.273
Distance ($d + h$), nm	32.26	24.37	6.714	−12.17	−14.9	−17.64
Embracing angle φ, °	6.92	7.77	9.40	10.88	11.08	11.28

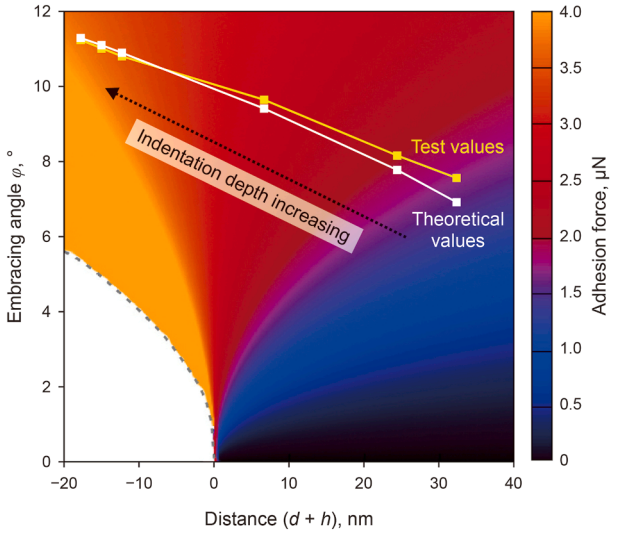


Fig. 16. Theoretical values of adhesion force at different embracing angles φ and distance ($d + h$).

The theoretical values of the adhesion force were calculated at φ = 0–12° with a distance ($d + h$) ranging from −20 nm to 40 nm to clearly understand the effect of indentation depth on adhesion force (Fig. 16). The black spot is the theoretical adhesion force under different contact forces, calculated according to the parameters inTable 2and Table 3 and the QLL-deformation capillary bridge model. The results demonstrated that there was a boundary condition in describing the relationship between φ and ($d + h$), which was determined by $R(\cos\varphi - 1) + (d + h) = 0$, as shown by the gray dotted line in Fig. 16. Near the boundary, the adhesion forces increased sharply and tended to infinity. The arrow in Fig. 16 shows the reasonable evolution of the φ, ($d + h$), and F_c with increasing indentation depth; that is, the increases in adhesion forces are induced by the increases in φ and the decreases in ($d + h$). This provides a reasonable explanation for the effects of nanoindentation and plastic deformation on the adhesion force between the mineral microsphere and the hydrate.

5. Conclusions

In this study, a modified AFM system was used to investigate the interfacial adhesive behaviors between clathrate hydrates and sediment microparticles, as well as SiO_2 microspheres. The effects of hydrate surface morphology, temperature, mineral microparticle size, contact force, contact time, and loading/unloading rate were systematically revealed. The conclusions are as follows.

(1) The clathrate hydrates in this study are polycrystalline materials with rough surfaces. Concave surfaces increase the width of the capillary liquid bridge between the hydrate and mineral microparticles, whereas convex surfaces reduce it. These surface characteristics directly influence the adhesion force.
(2) The influence of experimental parameters on adhesion force is determined by their distinct effects on the surface liquid layer. At larger contact forces and larger mineral microparticle sizes, plastic deformation in the hydrate lattice generates decomposition liquid, thickening the surface liquid layer and strengthening the capillary bridge, thus becoming the primary cause of the increased adhesion forces. Meanwhile, at higher temperatures, even when below the hydrate phase equilibrium temperature, the thickening of the QLL due to the premelting of the hydrate surface crystal dominates the increase in adhesion forces.
(3) The time dependence of adhesion force is linked to hydrate decomposition and reformation. During initial contact (<0.5 s), adhesion increases with longer time and higher loading rates due to QLL thickening and decomposition liquid formation, which together enhance the capillary bridge. During 0.5–2 s, adhesion decreases, likely because hydrate or ice reformation causes the surface layer to transition from a fluid-like to a more solid-like state, weakening the capillary bridge.
(4) By considering indentation depth and QLL thickness, a microscopic capillary liquid bridge model was optimized. The analysis clarifies that, under the experimental conditions, plastic deformation at the hydrate contact interface is approximately twice the elastic deformation during small-scale compression.

We believe these findings can contribute to solving the engineering roadblocks toward the industrial development of hydrate energy. Specifically, the study has revealed key factors governing the adhesion force between hydrates and particles. As an integral component of the cohesive forces among particles in hydrate reservoirs, adhesion force can directly influence the macromechanical behavior and sand production phenomena in

reservoirs when it is altered. This work provides a theoretical foundation for predicting and controlling the cohesion and stability of sediments, thereby helping to mitigate sand production risks during drilling operations. Future work will prioritize in situ comparative validation experiments under elevated-pressure conditions, as the systematic incorporation of pressure effects is expected to further refine and test the interfacial adhesion mechanisms proposed in this study.

CRediT authorship contribution statement

Wei Li: Writing – original draft, Methodology, Investigation, Conceptualization. **Zhi-Chao Liu:** Methodology, Formal analysis. **Feng-Yi Mi:** Writing – review & editing, Methodology. **Fang-Yu Shi:** Writing – review & editing. **Jiang-Tao Pang:** Writing – review & editing, Validation. **Zheng-Tao Tao:** Investigation. **Jia-Ni Hong:** Writing – review & editing. **Fu-Long Ning:** Writing – original draft, Supervision, Funding acquisition.

Declaration of competing interest

The authors declare that they have no known competing financial interests or personal relationships that could have appeared to influence the work reported in this paper.

Acknowledgements

This work was supported by the National Science Fund for Distinguished Young Scholars (grant numbers 42225207), the National Natural Science Foundation of China (grant number 42406219), and the China Postdoctoral Science Foundation (grant number 2024M763052).

References

Aman, Z.M., Brown, E.P., Sloan, E.D., et al., 2011. Interfacial mechanisms governing cyclopentane clathrate hydrate adhesion/cohesion. Phys. Chem. Chem. Phys. 13 (44), 19796–19806. https://doi.org/10.1039/c1cp21907c.

Aman, Z.M., Koh, C.A., 2016. Interfacial phenomena in gas hydrate systems. Chem. Soc. Rev. 45 (6), 1678–1690. https://doi.org/10.1039/c5cs00791g.

Brand, R.P., Mandemaker, L.D.B., Delen, G., et al., 2018. Behavior of a metal organic framework thin-film at elevated temperature and pressure as studied with an autoclave-inserted atomic force microscope. ChemPhysChem 19 (18), 2397–2404. https://doi.org/10.1002/cphc.201800284.

Butt, H.J., Kappl, M., 2009. Normal capillary forces. Adv. Colloid Interface Sci. 146 (1), 48–60. https://doi.org/10.1016/j.cis.2008.10.002.

Cao, P.Q., Sheng, J., Wu, J.Y., et al., 2021. Mechanical creep instability of nanocrystalline methane hydrates. Phys. Chem. Chem. Phys. 23 (5), 3615–3626. https://doi.org/10.1039/D0CP05896C.

Cheng, Z.C., Sun, L.T., Liu, Y.Y., et al., 2023. Study on the micro–macro kinetic and amino acid-enhanced separation of CO_2–CH_4 via sII hydrate. Renew. Energy 218, 119350. https://doi.org/10.1016/j.renene.2023.119350.

Corona-Arroyo, M.A., López-Valdivieso, A., Song, S., 2018. Contact angle and vacuum floatability of ultrafine size particles. Separ. Sci. Technol. 53 (6), 999–1005. https://doi.org/10.1080/01496395.2017.1405981.

Farrando-Perez, J., Balderas-Xicohtencatl, R., Cheng, Y., et al., 2022. Rapid and efficient hydrogen clathrate hydrate formation in confined nanospace. Nat. Commun. 13, 5953. https://doi.org/10.1038/s41467-022-33674-2.

Gelman Constantin, J., Gianetti, M.M., Longinotti, M.P., et al., 2018. The quasi-liquid layer of ice revisited: The role of temperature gradients and tip chemistry in AFM studies. Atmos. Chem. Phys. 18 (20), 14965–14978. https://doi.org/10.5194/acp-18-14965-2018.

Green, C.P., Lioe, H., Cleveland, J.P., et al., 2004. Normal and torsional spring constants of atomic force microscope cantilevers. Rev. Sci. Instrum. 75 (6), 1988–1996. https://doi.org/10.1063/1.1753100.

Guo, T.K., Wang, Y.P., Tan, B.J., et al., 2024. Research on productivity of stimulated natural gas hydrate reservoir. Renew. Energy 225, 120240. https://doi.org/10.1016/j.renene.2024.120240.

Guo, W., Li, Y.M., Jia, R., et al., 2023. Experimental study on mechanical properties of pore-filling and fracture-filling clayey silt hydrate-bearing sediments. Energy 284, 129354. https://doi.org/10.1016/j.energy.2023.129354.

Harrison, A.J., Corti, D.S., Beaudoin, S.P., 2015. Capillary forces in nanoparticle adhesion: A review of AFM methods. Part. Sci. Technol. 33 (5), 526–538. https://doi.org/10.1080/02726351.2015.1045641.

He, Z.X., Zhang, F., Ding, P.B., et al., 2025. Analysis of seismic dispersion and attenuation for gas-hydrate formations in the South China Sea. Pet. Sci. 22 (8), 3279–3292. https://doi.org/10.1016/j.petsci.2025.05.008.

Hill, T.M., Paull, C.K., Critser, R.B., 2012. Glacial and deglacial seafloor methane emissions from pockmarks on the northern flank of the storegga slide complex. Geo Mar. Lett. 32 (1), 73–84. https://doi.org/10.1007/s00367-011-0258-7.

Hong, J.N., Tian, Y., Liang, T.C., et al., 2024. Imaging surface structure and premelting of ice Ih with atomic resolution. Nature 630 (8016), 375–380. https://doi.org/10.1038/s41586-024-07427-8.

Hu, S.J., Koh, C.A., 2017. Interfacial properties and mechanisms dominating gas hydrate cohesion and adhesion in liquid and vapor hydrocarbon phases. Langmuir 33 (42), 11299–11309. https://doi.org/10.1021/acs.langmuir.7b02676.

Huang, X.B., Liu, F.B., Zhang, P.X., et al., 2023. Application of microgel latex in water-based drilling fluid to stabilize the fractured formation. Geoenergy Sci. Eng. 228, 212016. https://doi.org/10.1016/j.geoen.2023.212016.

Kim, B., 2022. Tracing marine gas hydrate destabilization with molecular fossils. Nat. Rev. Earth Environ. 3 (11), 740. https://doi.org/10.1038/s43017-022-00343-3.

Kong, Q.W., Wang, Z.Y., Pei, J.H., et al., 2025. An improved high-efficiency anti-agglomerant for avoiding hydrate flow barriers in high water-cut systems: Flowloop investigation and mechanisms. Sci. China Chem. 68 (6), 2691–2711. https://doi.org/10.1007/s11426-024-2371-9.

Lai, T.M., Chen, Y.G., Fang, B., et al., 2022. Decrease in adhesion force at silica-mica interface with short contact time due to dynamic formation process of liquid bridge revealed on an AFM. J. Adhes. 98 (10), 1501–1519. https://doi.org/10.1080/00218464.2021.1924154.

Lai, T.M., Meng, Y.G., 2018. Time-dependent dynamic behaviors of a confined liquid to achieve tailored adhesion force with repeated contacts revealed by atomic force microscopy. Langmuir 34 (50), 15211–15227. https://doi.org/10.1021/acs.langmuir.8b03164.

Li, E., Wang, Z.Y., Zhang, Y., et al., 2026a. Microscopic forces between methane hydrate particle and droplet-wetted sand grain surface in a high-pressure system: Experiments and mechanisms. Pet. Sci. 23 (5), 2963–2975. https://doi.org/10.1016/j.petsci.2025.11.042.

Li, W., Fang, B., Tao, Z.T., et al., 2024. Probing the instability of surface structure on solid hydrates: A microscopic perspective through experiment and simulation. Appl. Surf. Sci. 648, 158971. https://doi.org/10.1016/j.apsusc.2023.158971.

Li, W., Pang, J.T., Peng, L., et al., 2023a. Microscopic insights into the effects of anti-agglomerant surfactants on surface characteristics of tetrahydrofuran hydrate. Energy Fuel. 37 (5), 3741–3751. https://doi.org/10.1021/acs.energyfuels.2c04254.

Li, Y.L., Dong, L., Wu, N.Y., et al., 2021. Influences of hydrate layered distribution patterns on triaxial shearing characteristics of hydrate-bearing sediments. Eng. Geol. 294, 106375. https://doi.org/10.1016/j.enggeo.2021.106375.

Li, Y.L., Ning, F.L., Xu, M., et al., 2023b. Experimental study on solid particle migration and production behaviors during marine natural gas hydrate dissociation by depressurization. Pet. Sci. 20 (6), 3610–3623. https://doi.org/10.1016/j.petsci.2023.05.018.

Li, Y.L., Zhou, Y., Zhang, Z.C., et al., 2026b. Stress-induced melting controlled failure mechanisms of methane hydrate. Adv. Sci. 13 (10), e18367. https://doi.org/10.1002/advs.202518367.

Lin, Y.W., Li, T., Liu, S.Y., et al., 2023. Interfacial mechanical properties of tetrahydrofuran hydrate-solid surfaces: Implications for hydrate management. J. Colloid Interface Sci. 629, 326–335. https://doi.org/10.1016/j.jcis.2022.09.081.

Lin, Y.W., Zhou, Z.Y., Song, Z.X., et al., 2024. Insights into the mechanical stability of tetrahydrofuran hydrates from experimental, machine learning, and molecular dynamics perspectives. Nanoscale 16 (12), 6296–6308. https://doi.org/10.1039/d3nr04940j.

Liu, C.W., Zhou, C.R., Li, M.Z., et al., 2023. Direct measurements of the interactions between methane hydrate particle-particle/droplet in high pressure gas phase. Fuel 332, 126190. https://doi.org/10.1016/j.fuel.2022.126190.

Luo, Q., Li, W., Liu, Z.H., et al., 2024. Research progress on micro-force measurement of a hydrate particle system. Pet. Sci. 21 (4), 2169–2183. https://doi.org/10.1016/j.petsci.2024.03.017.

Luo, Q., Liu, Z.H., Dou, X.F., et al., 2026. Effect of weak consolidation process of liquid bridge on interparticle mechanical behavior of clathrate hydrate. Pet. Sci. 23 (4), 1625–1635. https://doi.org/10.1016/j.petsci.2025.11.038.

Nguyen, N.N., Berger, R., Kappl, M., et al., 2021. Clathrate adhesion induced by quasi-liquid layer. J. Phys. Chem. C 125 (38), 21293–21300. https://doi.org/10.1021/acs.jpcc.1c06997.

Nguyen, N.N., Nguyen, C.V., Nguyen, T.A.H., et al., 2022. Surface science in the research and development of hydrate-based sustainable technologies. ACS Sustainable Chem. Eng. 10 (13), 4041–4058. https://doi.org/10.1021/acssuschemeng.2c00028.

Ning, F.L., Yu, Y.B., Kjelstrup, S., et al., 2012. Mechanical properties of clathrate hydrates: Status and perspectives. Energy Environ. Sci. 5 (5), 6779–6795. https://doi.org/10.1039/c2ee03435b.

Pang, X.Q., Jia, C.Z., Xu, Z., et al., 2025. Application of the whole petroleum system in the evaluation of the global natural gas hydrate resource. Petrol. Explor. Dev. 52 (2), 301–315. https://doi.org/10.1016/S1876-3804(25)60568-4.

Phan, A., Stoner, H.M., Stamatakis, M., et al., 2022. Surface morphology effects on clathrate hydrate wettability. J. Colloid Interface Sci. 611, 421–431. https://doi.org/10.1016/j.jcis.2021.12.083.

Qureshi, M.F., Zheng, J., Khandelwal, H., et al., 2022. Laboratory demonstration of the stability of CO_2 hydrates in deep-oceanic sediments. Chem. Eng. J. 432, 134290. https://doi.org/10.1016/j.cej.2021.134290.

Taylor, C.J., Dieker, L.E., Miller, K.T., et al., 2007. Micromechanical adhesion force measurements between tetrahydrofuran hydrate particles. J. Colloid Interface Sci. 306 (2), 255–261. https://doi.org/10.1016/j.jcis.2006.10.078.

Thornton, B.F., Stranne, C., 2023. Flammable ice of profit and doom. Nat. Chem. 15, 294. https://doi.org/10.1038/s41557-022-01132-7.

Vlasic, T.M., Servio, P.D., Rey, A.D., 2019. THF hydrates as model systems for natural gas hydrates: Comparing their mechanical and vibrational properties. Ind. Eng. Chem. Res. 58 (36), 16588–16596. https://doi.org/10.1021/acs.iecr.9b02698.

Wang, D.D., Ning, F.L., Lu, J.G., et al., 2021. Reservoir characteristics and critical influencing factors on gas hydrate accumulations in the shenhu area, South China Sea. Mar. Petrol. Geol. 133, 105238. https://doi.org/10.1016/j.marpetgeo.2021.105238.

Wang, F., Ma, R., Xiao, S., et al., 2022a. Anti-gas hydrate surfaces: Perspectives, progress and prospects. J. Mater. Chem. A 10 (2), 379–406. https://doi.org/10.1039/d1ta08965j.

Wang, S.L., Fan, S.S., Lang, X.M., et al., 2020. Particle size dependence of clathrate hydrate particle cohesion in liquid/gaseous hydrocarbons. Fuel 259, 116201. https://doi.org/10.1016/j.fuel.2019.116201.

Wang, W.Y., Zhou, C.R., Liu, C.W., et al., 2022b. Experimental investigation of the adhesion forces/strengths of cyclopentane hydrate in a gas phase. Fuel 323, 124359. https://doi.org/10.1016/j.fuel.2022.124359.

Wu, J.Y., Ning, F.L., Trinh, T.T., et al., 2015. Mechanical instability of monocrystalline and polycrystalline methane hydrates. Nat. Commun. 6, 8743. https://doi.org/10.1038/ncomms9743.

Xue, H., Li, L., Wang, Y., et al., 2024. Probing the critical nucleus size in tetrahydrofuran clathrate hydrate formation using surface-anchored nanoparticles. Nat. Commun. 15, 157. https://doi.org/10.1038/s41467-023-44378-6.

Yamamoto, K., Wang, X.X., Tamaki, M., et al., 2019. The second offshore production of methane hydrate in the nankai trough and gas production behavior from a heterogeneous methane hydrate reservoir. RSC Adv. 9 (45), 25987–26013. https://doi.org/10.1039/C9RA03140E.

Yang, Z.M., Jiang, Y.F., Chen, B.B., et al., 2025. Study on the CO_2 hydrate distribution and seepage flow characteristics within NGH reservoirs. J. Energy Chem. 110, 681–692. https://doi.org/10.1016/j.jechem.2025.07.029.

Ye, J.L., Qin, X.W., Xie, W.W., et al., 2020. The second natural gas hydrate production test in the South China Sea. China Geol. 3 (2), 197–209. https://doi.org/10.31035/cg2020043.

Yu, Y.S., Zhang, X.W., Liu, J.W., et al., 2021. Natural gas hydrate resources and hydrate technologies: A review and analysis of the associated energy and global warming challenges. Energy Environ. Sci. 14 (11), 5611–5668. https://doi.org/10.1039/d1ee02093e.

Zhang, A.Y., Cai, M., Wei, N., et al., 2024. Analysis of sensitivity to hydrate blockage risk in natural gas gathering pipeline. Pet. Sci. 21 (4), 2723–2733. https://doi.org/10.1016/j.petsci.2024.01.016.

Zhao, Y.J., Hu, W., Dou, X.F., et al., 2024. Experimental investigation on the geological responses and production behaviors of natural gas hydrate-bearing sediments under various hydrate saturations and depressurization strategies. Appl. Energy 374, 123952. https://doi.org/10.1016/j.apenergy.2024.123952.